

ULRIKE HOMBERG, DANIEL BAUM, STEFFEN PROHASKA,
JENS GÜNSTER, STEFANIE KRAUSS-SCHÜLER

**Adapting trabecular structures for 3D
printing: an image processing approach
based on μ CT data**

Zuse Institute Berlin
Takustr. 7
14195 Berlin
Germany

Telephone: +49 30-84185-0
Telefax: +49 30-84185-125

E-mail: bibliothek@zib.de
URL: <http://www.zib.de>

ZIB-Report (Print) ISSN 1438-0064
ZIB-Report (Internet) ISSN 2192-7782

Adapting trabecular structures for 3D printing: an image processing approach based on μ CT data

U Homberg¹, D Baum¹, S Prohaska¹, J Günster²,
S Krauß-Schüler²

¹ Zuse Institute Berlin (ZIB), Department Visual Data Analysis, Takustr. 7,
14195 Berlin, Germany

² BAM Federal Institute for Material Research and Testing, Division Ceramic
Processing and Biomaterials, Unter den Eichen 44–46, 12203 Berlin, Germany

E-mail: homberg@zib.de jens.guenster@bam.de

Abstract. Materials with a trabecular structure notably combine advantages such as lightweight, reasonable strength, and permeability for fluids. This combination of advantages is especially interesting for tissue engineering in trauma surgery and orthopedics. Bone-substituting scaffolds for instance are designed with a trabecular structure in order to allow cell migration for bone ingrowth and vascularization. An emerging and recently very popular technology to produce such complex, porous structures is 3D printing. However, several technological aspects regarding the scaffold architecture, the printable resolution, and the feature size have to be considered when fabricating scaffolds for bone tissue replacement and regeneration.

Here, we present a strategy to assess and prepare realistic trabecular structures for 3D printing using image analysis with the aim of preserving the structural elements. We discuss critical conditions of the printing system and present a 3-stage approach to adapt a trabecular structure from μ CT data while incorporating knowledge about the printing system. In the first stage, an image-based extraction of solid and void structures is performed, which results in voxel- and graph-based representations of the extracted structures. These representations not only allow us to quantify geometrical properties such as pore size or strut geometry and length. But, since the graph represents the geometry and the topology of the initial structure, it can be used in the second stage to modify and adjust feature size, volume and sample size in an easy and consistent way. In the final reconstruction stage, the graph is then converted into a voxel representation preserving the topology of the initial structure. This stage generates a model with respect to the printing conditions to ensure a stable and controlled voxel placement during the printing process.

PACS numbers: 07.05.Pj, 81.05.Mh, 81.05.Rm, 87.85.J, 87.85.Lf

Submitted to: *Biomedical Physics & Engineering Express*

Keywords: trabecular structures, image-based analysis, additive manufacturing, printability

1. Introduction

Cellular materials are highly porous, consist of open and closed cells, and can be characterized by a network of struts and plates. They are present in many biological materials, such as cancellous bone [1], wood [2], marine skeletons [3], porcupine quills [4] or toucan beaks [5], and combine strength with low weight and, in case of open cells, enable fluid flow. This notable combination of properties makes cellular materials interesting, in particular for tissue engineering in trauma surgery and orthopedics. Scaffolds used to replace or repair bone tissue, for instance, are designed with a cellular structure, which must provide both mechanical function for proper load transfer and porosity for cell migration and nutrient supply [6]. Additive Manufacturing (AM), especially 3D printing, can produce such scaffolds on demand, even for irregular and complex anatomical shapes.

Scaffold design including porosity or strut geometry plays an important role in the successful application of the scaffolds. There are several design approaches on scaffold architecture: simulation-based approaches and methods based on topology optimization model scaffolds for specific degrees and values of stiffness [7], diffusivity [8], and permeability [9] that allow an efficient bone regeneration. In other studies, measures like porosity [10], geometrical parameters such as pore size [11] and feature orientation [12] are controlled by means of computer-aided design, which mostly result in regular and repeated patterns in the structures. Image-based approaches [13] make use of, e.g., CT data to extract and copy the acquired structures. In other disciplines, image-based methods have been developed for porous materials in order to identify and analyze details of the acquired structure. Basic ideas of assessing both phases of porous materials comprise extracting and separating voluminous structure elements such as granules or pores in sands [14], sphere packings [15], and cement [16], as well as analyzing the pore space as a network-like structure as in rock [17], soil [18], and sandstone [19]. In the former case, watershed-based methods [20, 21] are a widespread and robust way to segment and separate touching objects. In case of pore network analysis, most approaches compute a skeletal representation of the pore network using thinning algorithms [22, 23]. The outcomes of both are identified structural elements of solid and pore structures, which not only allow for a quantitative analysis of their geometric properties, but can also provide a basis to access and manipulate the extracted elements.

In addition to the scaffold architecture, another important aspect in the process of AM of scaffolds is the printability of the modeled structures, e.g., the ability to produce the features as they have been modeled. This requires the consideration of

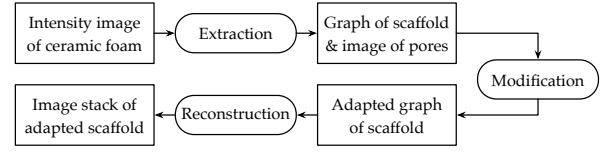


Figure 1. 3-stage approach to adapt trabecular structures for 3D printing.

further aspects related to the printing system. The printing resolution, powder material properties, e.g., particle size and shape, powder flowability [24], and specific parameters of the manufacturing process such as layer thickness, binder saturation, and drying time [25] influence the printing result. Combinations of these factors constitute the limitations of the printing systems. If, for instance, the printing resolution is too low, small features in direct vicinity may be printed as a single feature, whereas other features may even be ignored because of their small size. Podshivalo et al. [26] proposed a multi-scaling approach to adjust the feature sizes and feature details. We go one step further and consider possible changes that appear due to interpolations during the printing process. For example, the printing software virtually slices the designed 3D model into layers [27] according to the given printing parameters. This conversion step may change feature details of the models, so that the outcome is not clearly defined. To control the outcome, the model generation should take into account the conditions of the particular AM process.

Here, we discuss and present a strategy to mimic and transfer realistic trabecular structures to printing models while considering the conditions of the printing system. The method we present is a 3-stage image-based approach (Fig. 1) to adapt trabecular structures to the technological conditions of inkjet 3D printing based on μ CT data from a ceramic foam (Fig. 2). We first perform an image-based extraction of the structural elements of both solid and void phases to make the features accessible. This stage results in voxel- and graph-based representations of the extracted structural elements. In particular, the graph representation allows modifying the feature size, volume and sample size according to user-defined parameters. The final reconstruction stage then scan-converts the modified graph structure into a stack of binary images and generates the printing model. The second and third stages were developed with respect to the printing conditions ensuring stable and controlled voxel placement during the printing process. The two last stages require three user-defined parameters to incorporate knowledge about the printing process and to appropriately configure the modification and reconstruction process.

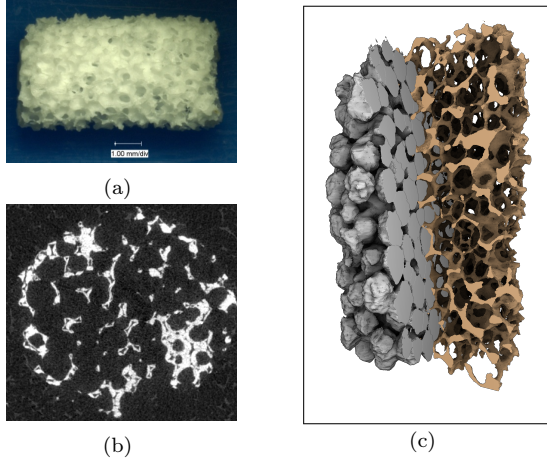


Figure 2. Replica of a ceramic foam: (a) photograph; (b) single slice of the three-dimensional CT scan; (c) Volume rendering of solid (brown) and void (gray) structure.

2. Methods: Image-based Adaption

The approach we present here is a processing chain that adapts realistic trabecular structures from μ CT for 3D printing processes. The resulting model preserves the topology: it must contain all features and their connections in a printable size; and it must be configured to enable the reliable manufacturing of these features. For this purpose, we consider different aspects arising from the limitations of printing processes.

Size of features As already mentioned above, a printing resolution that is too low compared to the size of the features to be printed may cause undesired effects: small features being close to each other may be printed as a single feature, whereas other features may even be omitted due to their small size. These filigree structures need to be simplified and optimized while preserving the properties of the initial scaffold structure. Thus, it might be necessary to enlarge or thicken the features of the structure.

Voxel connectedness The scaffolds are supposed to be generated from biocompatible materials using powder-based AM. This technology first spreads a layer of powdered material and selectively inscribes the corresponding layer information by local compaction and gluing; these steps are iteratively repeated until the object is completed. The layer information is generated by slicing the 3D model into layers of uniform thickness, where each slice represents the respective cross-section of the sliced object in a binary image. During the printing process, the voxels of the 3D model are subsequently added to the real structure layer by layer. But not all voxels are automatically interconnected with each other when

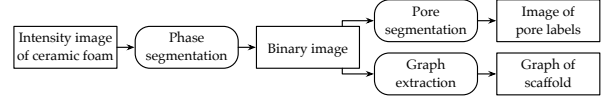


Figure 3. Steps of the image-based analysis.

arbitrary structures, such as those present in the μ CT data shown in Figure 2, are subdivided into individual printable voxels. On the other hand, real structures cannot contain disconnected voxels. But to obtain reasonable mechanical properties, all voxels should share as much surface area with adjacent voxels as possible. In terms of voxel connectedness, the voxels need to be 6-adjacent; the thinnest struts are assumed to be stable when they are produced as a sequence of 6-adjacent dots.

Deposition control To ensure the first two aspects, the voxels of the model must be fabricated as defined by the model. But the layer thickness and the minimum lateral pixel size, which can be defined in plane of each layer by adding material binder, determine the technical limits for the minimum voxel size. For 3D printing, it makes sense to define the voxels by the minimum value on a regular grid in three-dimensional space that can be resolved by the respective printing technology; otherwise the software of the printer may interpolate the positions where to deposit the material binder according to the technical conditions of the system. This may lead to leaving out or adding dots at undesired positions. Then, the adjacency of the printed dots might no longer be guaranteed. Hence, the printing model must fulfill these parameters to ensure that the printer accurately fixes the material at the desired positions.

To set up the model correctly, we incorporate knowledge about the printing process via three user-defined parameters:

- the sample size,
- the feature thickness, and
- the voxel size.

2.1. Extracting the structure elements

As described above, the first stage of our processing chain extracts the structural elements in order to make them accessible. This stage consists of a set of existing image processing methods, which are combined to process CT scans of ceramic foams. These scans were acquired at a resolution of $12\ \mu\text{m}$. Figure 2(c) shows a volumetric visualization of the acquired structures: the solid and the pore structure. To assess these complex structures, this part of our processing chain comprises three tasks (Fig. 3): segmenting the two

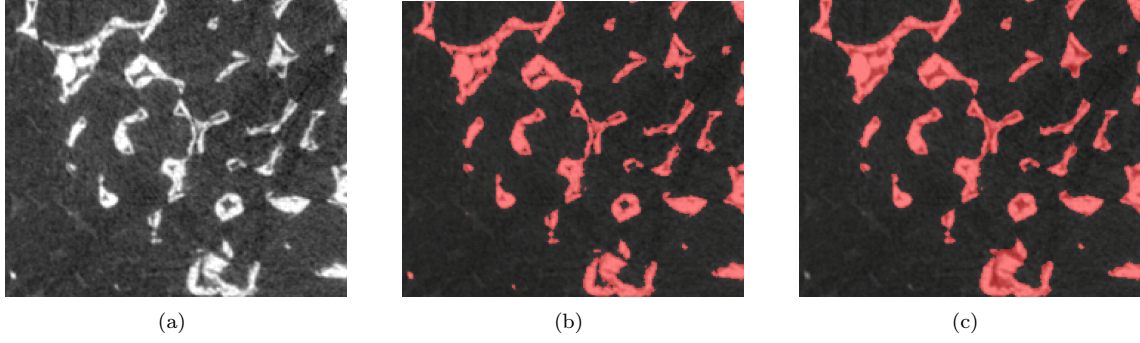


Figure 4. Two-phase segmentation: (a) slice detail of original data; (b) threshold segmentation; (c) filled main component.

phases, extracting the pores, and extracting the scaffold network.

2.1.1. Two-phase segmentation

We start with the determination of the two phases: The three-dimensional image domain $I \subset \mathbb{R}^3$ needs to be segmented into foreground (solid structure) $F \subset I$ and background (pore space) $B = I \setminus F$.

The segmentation process we propose is based on the following observations about the initial data (Fig. 4(a)): (i) The density of the solid is high compared to the density of air. (ii) The solid is a hollow structure due to the replication process. This means that the solid consists of thin walls and contains inner voids where the surrounding walls appear to be fragmented (not closed). These voids need to be closed to preserve the data integrity. (iii) The solid structure is a single connected component. However, the CT scans also contain further regions with high density that are caused by the sample fixture. These regions are small and separated from the actual structure. Therefore, they are easy to identify and can be removed without any de-noising procedure. These observations let us deduce a simple segmentation process consisting of the following steps.

Thresholding Because of the good contrast of the images, a simple binary threshold segmentation can be applied. This results in a first segmentation that separates the two phases into foreground and background; the segmented material phase does not include inner voids (Fig. 4(b)).

Material closing The material walls will be closed via dilation and erosion. The remaining inner voids can then be filled by applying a procedure that fills all background voxels within the material walls, which are not connected with the boundary of the data set.

Removing blobs Finally, undesired small regions are removed: a connected component analysis detects all

the separated regions. Then, a volume measurement of these regions allows one to identify the largest one, which is the desired structure. All other connected components are removed.

The result of this pipeline is a scalar field with a binary segmentation where the voxels of the foreground F are set to 1 and thus depict the complete region of the solid structure.

2.1.2. Pore segmentation

For reasons of deriving statistics on the pores as well as on the relation between pore space and solid, in this step, the pores are characterized and separated by means of the 3D distance function [28]. The starting point is the two-phase segmentation from the previous step. In this binary segmentation, the background B comprises the pores formed by the solid structure, but it also contains the space surrounding the entire sample, which needs to be differentiated for statistical clearness.

Distance map The basic step is to compute the signed distance function $f_D : I \rightarrow \mathbb{R}$ according to the boundary between foreground F and background B . Each point in the pore space is assigned the distance to its nearest point of the material phase.

$$f_D(p) = \begin{cases} \min_{q \in F} \|p - q\|, & \text{if } p \in B \\ -\min_{q \in B} \|p - q\|, & \text{if } p \in F \end{cases} \quad (1)$$

The extremal structures of the distance function f_D can be used to describe the pores. For this purpose, we make use of the definition of pore space elements based on the critical points c and the stable and unstable manifolds of the critical points $S(c)$ and $U(c)$ that we presented in detail in previous work [29]. The pore centers are located at the local maxima c_{max} of distance function f_D and the pore bodies are a subset of the stable manifolds of the corresponding maxima ($S(c_{max})$). This means that all points of the pore space B that end in a specific maximum c_{max} when following the steepest ascent belong to $S(c_{max}) \cap B$. Hence, the

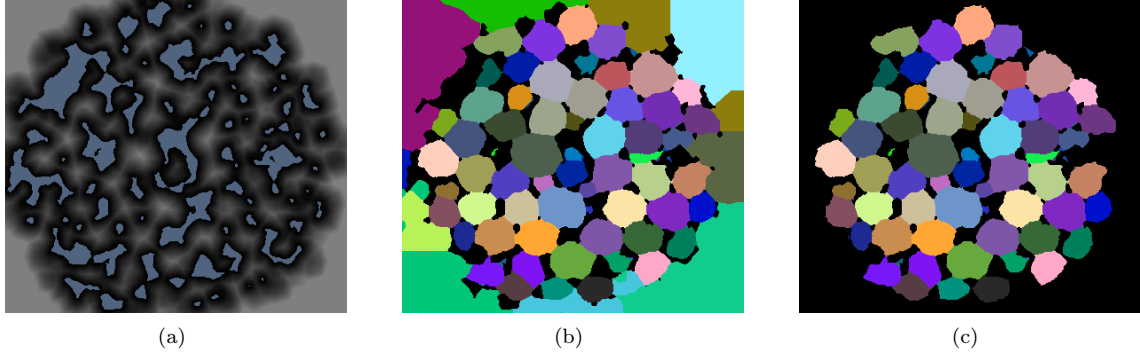


Figure 5. Pore segmentation: (a) distances (gray) to the boundary of the segmented material (blue); (b) segmented regions; (c) semi-automatically cleaned pores.

voxels of a pore body can be determined by labeling the voxels according to the maximum they belong to.

Hierarchical watershed segmentation This step detects all the regions that correspond to a subset of the basins $S(c_{max}) \cap B$. Furthermore, it deals with the fact that the pores might be elongated and have multiple maxima within a single pore. A decomposition of the pore space can be computed using a hierarchical watershed segmentation [30] that detects and labels the maxima and then propagates them in the order of decreasing distances along all points that have non-negative distance values. The hierarchy is built based on tuples of two neighbored maxima and their connecting 2-saddle point. It lets the user merge neighboring regions to reduce over-segmentations.

Our merge criterion is based on the persistence of the features of the distance function f_D , in particular, the maxima c_{max} and the index 2-saddle points c_{s2} . To take into account the varying pore sizes, we introduce a locally relative persistence that is computed for each hierarchical tuple (c_{max1}, c_{max2}) and their hierarchical 2-saddle point c_{s2} .

$$t_p = \frac{\min_{x \in [c_{max1}, c_{max2}]} d(x) - d(c_{s2})}{\min_{x \in [c_{max1}, c_{max2}]} d(x)} \quad (2)$$

The segmentation result decomposes the background into a set of regions B_i with $B = \cup B_i$ that mark the separated pore bodies but also regions of the boundary space surrounding the sample.

Semi-automatic removal of boundary space To obtain only the regions of the pore bodies, the regions of the surrounding space still need to be removed. They are characterized by their irregular shape and their connection to the image boundary, while the actual pores are of ellipsoid shape and enclosed by the material phase and neighboring pores. An interactive procedure supports the user to mark these regions through manual picking. A subsequent automatic step

fills these regions with a unique label, such that the background now consists of a region $B_S \subset B$ that comprised the sample surrounding space and a set of disjoint regions R_i with $\cup R_i = B \setminus B_S$ describing the separated pore bodies.

2.1.3. Graph extraction and representation

The foam has a regular structure that forms similarly shaped pores. Modifications of the structure elements and their properties need to be placed consistently over the entire structure. To identify elements and their properties, we need a representation that encodes the spatial arrangement and connectedness of the struts and the nodes as well as their properties like thickness.

For this purpose, we build a graph that represents the scaffold structure with its elements and their properties. An appropriate representation approximates the medial axis of the trabecular structure, such that the distance to the surrounding material boundary is maximal. Then, the distance describes the thickness of the material at each point.

The following sequence of processing steps computes the graph that represents the scaffold structure, starting from the binary segmentation of the two-phase segmentation.

Skeletonization We make use of the shape properties of the scaffold elements: The struts are elongated and symmetric in their cross-sections and allow the application of thinning algorithms. Furthermore, one of the tasks of the scaffold is to provide stability in itself and to distribute the load over the strut construction. In the latter case, dead ends do not contribute to load balancing, therefore, they will be ignored in this study. Hence, a distance-ordered homotopic thinning that preserves the homotopy of the trabecular structure is applied [31] to the material phase (Fig. 6(a)). The result is a sparse binary image where only the voxels that belong to the skeleton are set to 1, depicted by the red voxels in Figure 6(b).

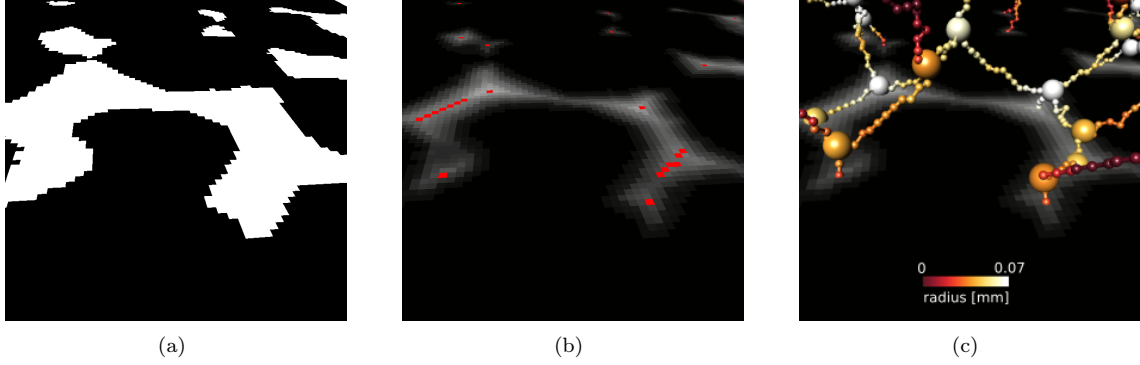


Figure 6. Graph extraction: slice detail with (a) segmented material; (b) distances within the material (gray) and skeleton voxels (red); (c) scan-converted graph with color-coded thickness.

Distance map Independently of the thinning, the unsigned distance function on the binary segmentation to the materials boundary is computed, where the distances within the material are now positive and the background is ignored: $f_D^+(p) = \min \|p - q\|$, with $p \in F, q \in B$, and $f_D^+(p) = 0$, with $p \in B$. Assuming that the thinned skeleton approximates the medial skeleton, the distance along the skeleton voxels represent the maximal distances to the material boundary.

Scan conversion We construct a graph representation by converting the skeleton voxels into a graph $G = (V, E, P)$: The vertices $v_i \in V$ represent the connections of the struts and are located in the middle of the connection clusters. The edges $e_i \in E$ represent the struts; and the geometric course of the edges is given by the edge points $p_i \in P \subset \mathbb{R}^3$. Furthermore, each point p_i is assigned a weight $r_p \in \mathbb{R}$ that is the value of the distance function f_D^+ at the point location and is interpreted as the local thickness of the represented struts. Figure 6(c) shows a detail of the extracted graph, where the local thickness is depicted by the color coding along the edges.

2.2. Modifying the scaffold structure

The methods of the previous section extracted the elements of the solid structure and encodes their arrangement and other properties—they can be seen as a template for mimicking the initial structure. As described at the beginning of this section, the investigated structures may have features that are too small with respect to the designated printing parameters. The upcoming step allows modifying the extracted structure according to the discussed criterion of the *size of features* and incorporates user input for sample size and feature size.

Compared to the voxel-based representation of the segmented solid, the graph representation enables an effective access to (i) the elements of the graph (struts and strut connections), (ii) their geometric

information (position, course, and arrangement), and (iii) their weights (thickness information). Therefore, this graph provides a good basis to modify the elements of the scaffold in a consistent way and makes it easy to define a modification criterion and modification conditions, for example, increasing the radius at very thin locations.

2.2.1. Modification tasks

We propose two simple ways of modification, which can be configured by the user: resizing the sample (R) and setting the thickness of the struts (T). The starting point is the graph G described in Section 2.1.3.

Resizing To compute a desired sample size, the extracted graph G will be resized according to the user setting, which is given by the destination sample height. The geometry of the graph and the point weights, namely the thickness information, are scaled to the desired size resulting in graph G_R .

Modifying the thickness This step modifies the thickness information of each point $p \in P$ of the resized graph G_R . It is used to set a specific strength of the struts or a specific volume of the structure. The following section describes different modes of modification.

2.2.2. Thickening modes

We focus on simple modification strategies realized in different modes that change the thickness of the scaffold struts. For this purpose, the radius r_{p_i} of the edge points $p_i \in P$ of the resized graph G_R can be changed in order to obtain the modified graph G_{RT} following the criteria and conditions below. Figure 7 illustrates the different modes. The gray parts depict an example edge, its edge points, and the initial radius. The black lines denote the modified radius attributes.

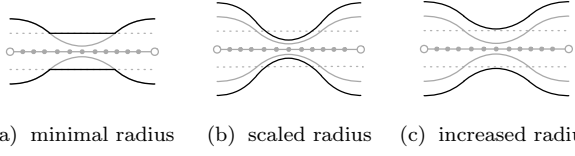


Figure 7. Illustration of the modification modes for a single graph edge (bright gray) connecting two vertices (empty circles) and running along the edge points (filled circles). The thickness information is depicted by the gray curve and the desired minimal thickness by the dotted lines. Possible results for the different modes are shown by the black lines.

Minimal thickening The thickness weights r_{p_i} of all points of the graph G_R that have a thickness smaller than the user-defined threshold $r_{p_i} < t_m$ are set to the minimal thickness t_m on the new graph G_{RT}^{min} , while the remaining weights will be preserved (Fig. 7(a)).

Scaling All weights r_{p_i} of each point $p_i \in P$ of the graph G_R are scaled by the user-defined factor s to obtain the new graph G_{RT}^{scale} with weights $r_{p_i}^{scale} = r_{p_i} \cdot s$ (Fig. 7(b)).

Increasing All weights r_{p_i} of the graph G_R are increased by a user-defined constant value c to obtain the modified graph G_{RT}^{incr} (Fig. 7(c)). The value c may be chosen as the radius difference between the minimal thickness of the graph G_R and the minimal thickness that is printable, for example.

Ratio-based thickening This mode iteratively computes the thickness parameter that creates a sample with a user-defined solid ratio when applying a specified mode from above (scaling, increasing or a combination of both with minimal thickness). It anticipates the results of the last part of our approach (Section 2.3) and, thus, makes use of the finally scan-converted voxelized scaffold: Each iteration creates the final voxelized scaffold for a thickness parameter and computes the solid ratio as the ratio of the solid voxels to the total number of voxels. The determination of the thickness parameter for the next iteration is realized by a binary search over a range of thicknesses guided by the ratio of the current iteration compared to the user-defined ratio. The iterations are then repeated until the user-defined solid ratio including a tolerance is reached.

2.3. Reconstructing the scaffold structure

The final part of our approach reconstructs the scaffold structure from the modified graph into a three-dimensional image, which then can be written into a stack of 2D images or triangulated to an STL file as input for the printing system. The reconstruction follows the discussed requirements of *voxel connectedness* and *dot control*, where the voxel

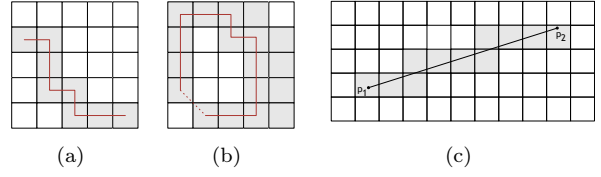


Figure 8. 2D illustration of 6-connectedness: (a) path of 6-connected voxels; (b) set of 6-connected voxels; (c) line segment (p_i, p_j) embedded in the according 6-connected voxel path.

connectedness is ensured by a specific scan conversion and the dot control handled by the third user input: the voxel size of the resulting data set. Here, the voxel size must not be smaller than the one of the printing system, so that, together with the previous modifications, all features are transformed to the image in a printable size and resolution.

The resized and modified graph G_{RT} will be scan-converted into a binary image using the reconstruction step $I_R : \mathbb{N}^3 \rightarrow \{0, 1\}$, where the size of the image $N_x \times N_y \times N_z$ is computed from the user-defined voxel size and the bounding box of graph G_{RT} including its weights, which are interpreted as the radius of spheres at the corresponding points. Regarding the printing process, the binary image describes where the printer will fix the material ($I_R(x) = 1$) and where not ($I_R(x) = 0$).

As described at the beginning of this section, one requirement is to set the material in a stable manner and that this setting corresponds to the 6-adjacency of the voxels. Since the struts are not only lines that have to be scan-converted but also volumetric tube-like structures with varying thickness, an extension of the condition of 6-adjacency is necessary. Following the formulations on neighborhood of Kaufman et al. [32], the ‘stable’ neighborhood for an arbitrary set of voxels can be formulated as follows: Two material voxels are 6-adjacent if they share a common face (considering a voxel to be a cuboid volume element centered at a sampling point of the data set). A 6-path is a sequence of consecutive pairs of 6-adjacent material voxels (Fig. 8(a)) and a volume of material voxels is 6-connected if there is a 6-path between any pair of material voxels (Fig. 8(b)). Thus, the set of the material voxels is ‘stable’ if all voxels of the set is 6-connected. That is, the scan conversion method only sets a material voxel if and only if a 6-connectedness to existing material voxels can be established.

Scan-converting the volumetric structure as a whole hampers finding rules for setting and leaving out material voxels while preserving the 6-connectedness. The proposed approach makes use of the elementary information of the graph $G_{RT}(E, V, P)$, where the set of vertices V and the set of edges E describe the connectedness of the strut network and the N points

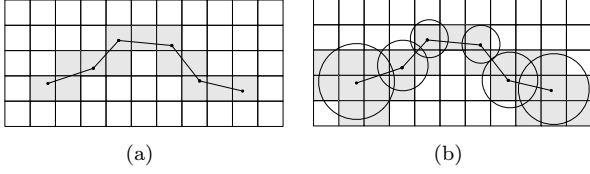


Figure 9. 2D illustration of 2-step scan conversion. The first step (a) ensures the 6-connected paths of the scan-converted line segments; the second step (b) adds a 6-connected set of voxels of the scan-converted weights of points.

$p_i \in P$, with $i = 1, \dots, N$, as well as their weights r_{p_i} encode the course of the struts and the thickness along the struts. In fact, the points describe linear line segments between sequential pairs (p_i, p_j) with $j = i + 1$ and the weights describe spheres with radius r_{p_i} centered at p_i . These two facts facilitate to control the 6-connectedness during a 2-step scan conversion: the first step maps the line segments with respect to the 6-adjacency (Fig. 9(a)); the second step exploits the convexity of spheres and adds the thickness to the line segments (Fig. 9(b)).

2.3.1. Scan-converting the line segments

Mapping the line segments builds the basis for marking the material voxels as one 6-connected component. The course of a line segment needs to be marked as a sequence of 6-adjacent voxels. For this purpose, we apply an algorithm that was originally intended for ray tracing in rendering tasks: Amanatides and Woo [33] proposed an efficient algorithm that traverses all voxels along a ray. In terms of our application, this approach can identify all voxels that the line segment touches (Fig. 8(c)).

Initialization Before scanning a line segment, the start and end points p_i and p_j will be assigned to the corresponding voxels v_i and v_j in the resulting image I_R . The voxel coordinates $v = (v_x, v_y, v_z) \in \mathbb{N}^3$ are computed from the point location $p = (p_x, p_y, p_z) \in \mathbb{R}^3$ related to the minimal coordinates of the bounding box $b_x^{min}, b_y^{min}, b_z^{min} \in \mathbb{R}$ of the entire graph and from the defined voxel size $s_x, s_y, s_z \in \mathbb{R}$:

$$v_a = \lfloor ((p_a - b_a^{min})/s_a) + 0.5 \rfloor, a \in \{x, y, z\} \quad (3)$$

with $a \in \{x, y, z\}$ to indicate the axis related component. Adding 0.5 and applying floor yields the discrete voxel coordinates.

Traveling along the line segment within the image grid requires the direction $d = \overrightarrow{p_i p_j} \in \mathbb{R}^3$ from the start point p_i to the end point p_j . The sign of the components of d determines the step increments or decrements $k_x, k_y, k_z \in \{-1, 0, 1\}$ when traversing the

voxels along the line:

$$k_a = \begin{cases} 1, & \text{if } d_a > 0 \\ -1, & \text{if } d_a < 0, a \in \{x, y, z\} \\ 0, & \text{else} \end{cases} \quad (4)$$

The sampling itself is guided by the following variables. $\Delta t_x, \Delta t_y, \Delta t_z \in \mathbb{R}$ is the portion of the line segment to cross the distance of one entire voxel depending on the axes.

$$\Delta t_a = \begin{cases} \text{abs}(s_a/d_a), & \text{if } d_a \neq 0 \\ \infty, & \text{else} \end{cases}, a \in \{x, y, z\} \quad (5)$$

$t_x, t_y, t_z \in \mathbb{R}$ determines the time to travel along the line segment per axis until the next voxel is reached. Initially, it is set to the portion of the line segment that describes the distance from the origin p to the voxel boundaries v_a^{min} and v_a^{max} of the voxel it is located in.

$$t_a = \begin{cases} \Delta t_a \cdot (v_a^{max} - p_a)/s_a, & \text{if } d_a > 0 \\ \Delta t_a \cdot (p_a - v_a^{min})/s_a, & \text{if } d_a < 0, \\ \infty, & \text{else} \end{cases}, a \in \{x, y, z\}. \quad (6)$$

Voxel traversal The traversal itself is then realized in an incremental loop (Algorithm 1) as proposed by Amanatides [33]. Here, the traversal algorithm is not used to determine the first object that intersects the ray. It is applied to determine all voxels along the line segment (p_i, p_j) as a 6-adjacent sequence and to mark them as material voxels in the reconstruction image I_R .

The loop starts at the voxel v_i that contains the start point p_i and follows the line segment by choosing the minimum $\min(t_x, t_y, t_z)$. The minimum indicates in which direction the next voxel boundary will be crossed. For this direction, for example x , the voxel coordinate is incremented by k_x in case of a positive x -component of the direction vector d or decremented in case of a negative x -component. The case of $d_a=0$ will not appear since t_a is initialized as infinite. Accordingly, the ‘travel time’ t_x is increased or decreased by Δt_x . This is repeated until the end voxel v_j of the line segment is reached.

Two facts guarantee that the line segment is scan-converted in a 6-adjacent way. (i) The parameters t_a indicate the distance to the next voxel facet and guide the algorithm to traverse the neighbor voxel that shares that facet. (ii) Even if the line crosses an edge or a corner of a voxel, the algorithm always processes the minimum of the t_a parameters. Thus, it traverses all neighbor voxels that share that edge or corner and creates a 6-connected line segment.

2.3.2. Scan-converting the spheres

The previous step only maps the skeleton of the modified scaffold graph onto the reconstruction image

Algorithm 1 Voxel traversal to scan-convert 6-connected line segments from points p_i to p_j . Adapted from Amanatides [33].

```

1: procedure VOXELTRAVERSAL
2:   input:  $p_i, p_j \in \mathbb{R}^3$ 
3:   output: List  $L \triangleright$  Voxel coordinates to be
      marked as material voxels

4:   initialize:
5:      $v_i, v_j \in \mathbb{R}^3 \triangleright$  start and end voxel of line
      segment (Eq. 3)
6:      $k_a \in \{-1, 0, 1\} \triangleright$  increments/decrements for
      voxel coordinates (Eq. 4)
7:      $\Delta t_a \in \mathbb{R} \triangleright$  distances to cross one voxel
      (Eq. 5)
8:      $t_a \in \mathbb{R} \triangleright$  distances to the next voxel
      boundary (Eq. 6)

9:    $w \leftarrow v_i$ 
10:  while  $w \neq v_j$  and  $w \in I$  do
11:    if  $t_x < t_y$  then
12:      if  $t_x < t_z$  then
13:         $w_x \leftarrow w_x + k_x$ 
14:         $t_x \leftarrow t_x + \Delta t_x$ 
15:      else
16:         $w_z \leftarrow w_z + k_z$ 
17:         $t_z \leftarrow t_z + \Delta t_z$ 
18:      end if
19:    else
20:      if  $t_y < t_z$  then
21:         $w_y \leftarrow w_y + k_y$ 
22:         $t_y \leftarrow t_y + \Delta t_y$ 
23:      else
24:         $w_z \leftarrow w_z + k_z$ 
25:         $t_z \leftarrow t_z + \Delta t_z$ 
26:      end if
27:    end if
28:     $\text{add}(L, w)$ 
29:  end while
30: end procedure

```

(Fig. 9(a)). As described above, the weights r_{p_i} of the points p_i can be interpreted as spheres with radius r_{p_i} centered at p_i . Scanning the spheres now adds the thickness information to the skeleton (Fig. 9(b)). This means, all voxels that have a distance from its center to any point p_i smaller than the corresponding radius r_{p_i} are marked as material voxels:

$$I_R(x) = \begin{cases} 1, & \exists p_i : \|x - p_i\| < r_{p_i}, p_i \in P \\ I_R(x), & \text{otherwise} \end{cases}, \quad (7)$$

$$I_R : \mathbb{N}^3 \rightarrow \{0, 1\}$$

Since the spheres are convex objects, all voxels covered by a sphere form a 6-connected component. Adding all spheres to the skeleton composes a set of 6-connected components. This composition produces neighbored pairs of material voxels that are locally only connected via an edge or a corner (dashed line in Fig. 8(b)),

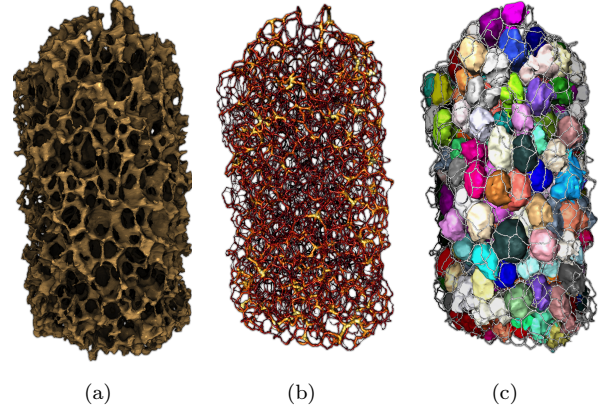


Figure 10. Results of image processing part for an entire data set: (a) segmented solid material; (b) extracted graph with color-coded thickness; (c) extracted pore bodies and graph.

but there exists at least one 6-path that connects them (solid line in Fig. 8(b)).

2.3.3. Remarks

The presented voxel traversal guarantees the 6-adjacency for all edges of the graph: since adjacent line segments as well as adjacent edges share an edge point or a vertex respectively, the entire skeleton of the scan-converted graph is guaranteed to be 6-connected.

The resolution of the destination image does not have any impact on the 6-connectedness: Even if the modification step results in a graph with line segments that have a thickness smaller than the destination voxel size, the line segments are still scan-converted as a 6-connected path. In this case, the resolution determines the minimal thickness of the features to be printed.

3. Results

The foam we analyzed was scanned using the micro-computed tomography scanner μ CT 42 by Scanco Medical AG (Switzerland). The steps of graph extraction, modification, and reconstruction were implemented as extension modules for Amira [34], a software system for visualization and data analysis. The computations were carried out on a desktop machine with 2 Quad-Core Intel Xeon (2.4GHz) and 64 GB memory.

We processed a sample of a ceramic foam (Fig. 2(a)) with a height of nearly 8 mm and a diameter of about 4 mm. The structure was scanned with a resolution of 12 μ m, which results in a data set with a size of $454 \times 412 \times 643$ voxels.

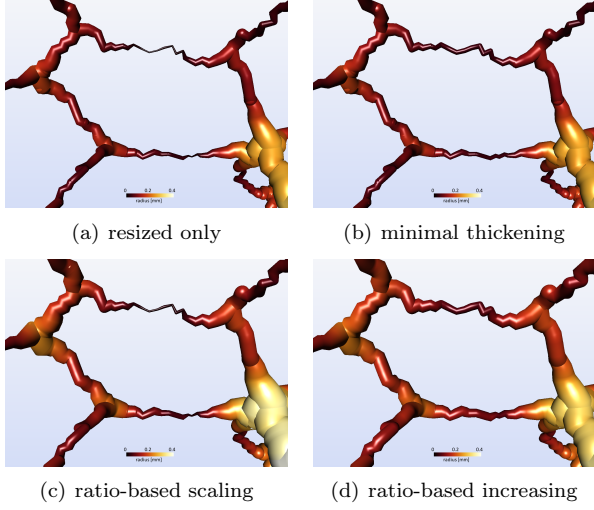


Figure 11. Graph detail computed with different thickening modes: (a) initial thickness; (b) setting minimal thickness; (c) scaling and (d) increasing the thickness. The thickness of the graph edges is scaled to one third of the actual thickness for clarity of illustration.

3.1. Extracted solid and pore structures

For the generation of a manipulated version of the initial structure, we first applied the extraction part by segmenting the material, computing the graph-based representation, and segmenting the individual pores.

The *phase segmentation* required the selection of the right intensity parameter for the threshold segmentation and resulted in a binary voxel data set (Fig. 10(a)). The step of finding the segmentation threshold and computing the further steps of this pipeline is interactive on a current work station. The *graph extraction* was applied to the binary segmentation. Figure 10(b) shows the resulting graph with scaled and color-coded thickness – from thin (dark red) to thick (yellow). The computation of the graph is parameter-free and took less than a minute for the data set. The *pore segmentation* (Fig. 10(c)) required a pre-computation for building the hierarchy of the watershed-based segmentation, which took less than 7 minutes. Then, the results for the varying persistence values were available within seconds.

Both the graph and the pore data set describe all important structural elements in a compact way. Information on the solid structure (i.e., length, diameter, and orientation of the struts) and the pore space (i.e., extent, volume, and orientation of pores) can easily be derived for quantification and comparison, which are, however, beyond the scope of this paper.

3.2. Modification and reconstruction

Based on the graph representation, we computed different modifications and scan-converted them into

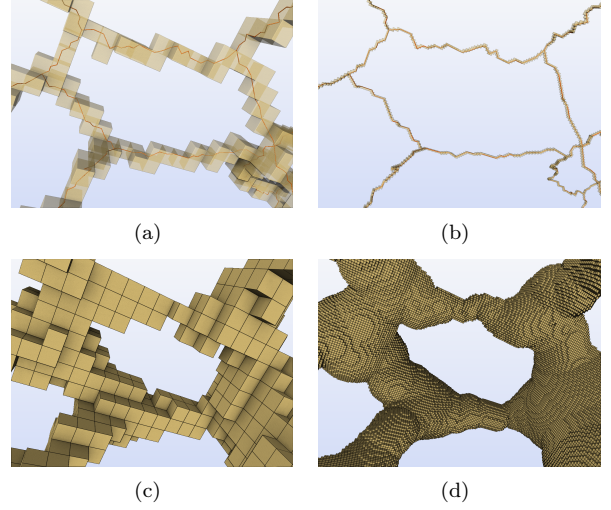


Figure 12. Reconstruction: scan-converted line segments for (a) $100\mu\text{m}$ and (b) $12\mu\text{m}$ in the upper row, scan-converted spheres for (c) $100\mu\text{m}$ and (d) $12\mu\text{m}$ in the lower row.

voxel data sets, which were then saved as a stack of images or a STL file. We generated the example data sets to demonstrate the tasks of resizing, thickening, and reconstructing. The examples were resized from 8 to 20 mm in height and then modified by the presented thickening modes.

Figure 11 illustrates the modification for a detail of the graph, where the thickness information is depicted by coloring and scaling along the edges. The extracted graph and its thickness information were up-scaled to the destination height; the thickness relations stay the same and can be used here for comparison with the subsequent modifications (Fig. 11(a)). Setting a minimal thickness changes only the parts of the struts that have a thickness below the user-defined threshold (see upper horizontal edge in Fig. 11(b)). The modes of scaling (Fig. 11(c)) and increasing (Fig. 11(d)) change all edges by a factor or a constant, respectively. The latter one was computed using the iterative ratio-based modification with respect to the solid-void ratio of the entire data set of the segmentation results. That is, the ratio was computed from the material phase and the void phase including the material surrounding parts of the data set — this allows us to easily check the destination ratio per iteration until the result fits the amount of volume of initial material phase.

Figure 12 shows the same graph detail as Figure 11 after scan-converting the modified graph. We chose two resolutions for the scan conversion to better illustrate the connectedness, the trade-off between resolution and accuracy, and the ability to mimic the initial structure. The data set shown in the left column was generated with a resolution of $100\mu\text{m}$ derived from the current resolution of powder printers, whereas the example shown in the right column was generated

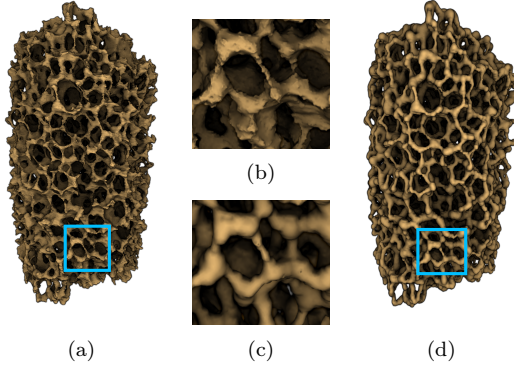


Figure 13. Reconstruction of the entire structure: (a) segmented initial structure (height of 8 mm) and (b) a zoom-in; (d) a reconstructed structure (re-sizing (20 mm), ratio-based increasing, scan-converting (12 μ m)) and a zoom-in (c).

with a resolution of 12 μ m, which corresponds to the resolution of the initial CT scan. It is obvious that a finer resolution allows a more accurate sampling of the scaffold structure encoded by the modified graph. Assuming that there were no restrictions to the resolution, the 12 μ m example demonstrates the ability of our concept to mimic the initial structure. Figure 13 compares the segmented foam (Fig. 13(a),(b)) and the reconstruction of the ratio-based increased scaffold (Fig. 13(c),(d)) in overview and detail.

4. Discussion

The presented graph concept is a compact description of the connectivity of the trabecular structure as well as of course and thickness of its structural elements. In addition, it enables a consistent definition of modification rules and provides a data structure as a basis for the upcoming scan conversion. However, the graph is designed to describe structures that mainly comprise tubular features, whereas cellular structures may contain features that differ from tube-like shapes. For example, the processed ceramic foam exhibits small sharp edges along the struts (Fig. 13(b)) and plate-like features at the connection of two struts (Fig. 14). These features represent a divergence from the tubular struts and are not completely reconstructed when scan-converting the graph into the voxel representation. This may lead to an underestimation of the material. Figure 15 illustrates this effect for the different modification modes. Figure 15(b) compares the segmented phase with the reconstructions after setting a minimal thickness. This mode keeps the majority of thickness relations of the resized graph, but exhibits a strong underestimation. The ratio-based methods (Fig. 15(c),(d)) iteratively find the right thickness parameter and result in reconstructions that have the

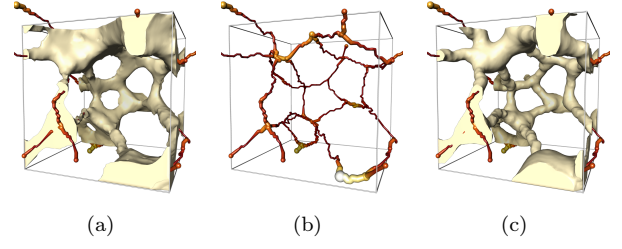


Figure 14. Differences between initial structure with flat extension at the strut connections and the tubular reconstruction: Cropped detail with (a) the segmented material of the initial structure, (b) graph that represents the segmented material including the color-coded thickness information (red: thin, yellow/white: thick), and (c) the material reconstructed from the graph representation.

same amount of material. These methods achieve a material compensation by construction: while sharp features are ignored, the scan conversion of the tubular representation fills cavities along the struts. For structures presented in this paper, our approach produces good approximations of the original structures. However, for structures that differ from tubular shapes more significantly, more information needs to be encoded on the graph. By means of a point-wise eigenvalue analysis, flat features can be detected in the CT scan and described by adding the extent (eigenvalues) and the orientation (eigenvectors) to the graph instead of only the radius.

The scan conversion is driven by the concept of 6-connectedness that produces a set of material voxels without any free and disconnected voxels. This concept ensures the conversion of end-to-end struts and, thus, the preservation of the topology of the entire structure up to a certain voxel size. The topology, of course, only can persist if the voxel size and the printer resolution allow resolving the features. For example, too large voxel sizes may lead to merged features. In such a case, it is not possible to transfer all features to the finally printed sample. By assuming a suitable printer resolution, our approach allows the user to control the voxel size, which then must be set to a voxel size that the printer can produce and does not cause the printer software to interpolate the positions for setting or leaving out the binder. The combination of 6-connectedness and correct voxel size can be seen as minimal configuration that preserves the topology, but it does not guarantee enough strength and stability along the end-to-end struts. To support this, a user-defined thickness can be set in the modification step to ensure a specific feature size beyond the 6-connectedness and the voxel size. Therefore, setting the parameters needs experience and knowledge about the printing system and the behavior of the printing materials.

The presented image-based methods that extract

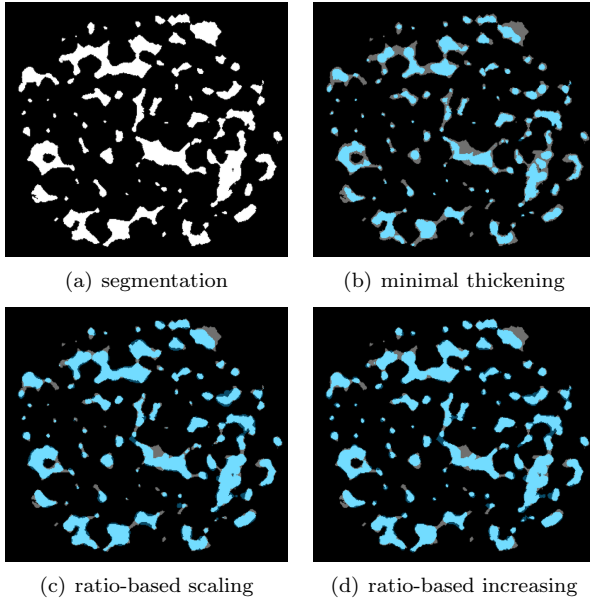


Figure 15. Reconstructions of different thickness modification: a selected xy-slice of the segmented scaffold structure (a) and overlays in blue for the reconstruction using minimal thickness (b), scaling (c), and increasing (d) the thickness.

the scaffold network and the pores are also applicable to data sets obtained from the reconstruction step as well as by re-scanning the printed scaffolds. This means, the graph of the scaffold and the voxel-based representation of the pores can additionally be used to compare the solid and pore structures of the initial sample, the voxel-based reconstruction, and the re-scanned printed result.

5. Conclusion and Future Work

This paper addresses the generation of models for bone-substituting scaffolds via inkjet 3D printing with improved printability of the contained structures. We aim to produce models of realistic structures that are printable while preserving the required properties such as stability and porosity to ensure load transfer and nutrient supply. The presented method is a 3-stage approach that allows users to control the generation of the model with respect to the conditions of the printing system. A trabecular structure will be extracted from μ CT data in the first stage to provide a basis for mimicking and adapting the structure. The second and third stages incorporate the three discussed aspects important for printability: size of features, deposition control, and voxel connectedness. The size of the features and the sample is defined by the user and handled during the modification step. Another user input is the voxel size, which directly correspond to the deposition issue and is considered during the

reconstruction step. The reconstruction step also handles the voxel connectedness and ensures that all features of the extracted and modified structures stay connected and are transferred to the printing model without loss.

The presented modification of the structures is computed on the solid-representing graph. It changes the thickness of the struts, which implicitly also changes the size and shape of the pores. These changes can not be characterized until the reconstruction is generated and the pore segmentation is computed again. However, if the graph represented both phases, the scaffold and the pore network, it might be used to construct an interactive tool to set up the properties for the two phases at the same. Tracking these changes and showing them during the modification step may help to even better control important properties such as stability and porosity.

With our approach, we propose a strategy to assess and adjust realistic structures for 3D printing using image analysis that focusses on trabecular structures for a start. Other kinds of structures would require the development of further appropriate compact representations. Given such appropriate representations, we believe that our proposed pipeline will be applicable to adapt a wide range of input structures to specific printing conditions.

References

- [1] Currey JD 2002 *Bones: structure and mechanics* Princeton university press
- [2] Gibson L J and Ashby M F 1997 *Cellular solids: structure and properties*
- [3] Aizenberg J, Weaver J C, Thanawala M S, Sundar V C, Morse D E, and Fratzl P 2005 Skeleton of *Euplectella* sp.: structural hierarchy from the nanoscale to the macroscale *Science* **309** 275–278
- [4] Yang W and McKittrick J 2013 Separating the influence of the cortex and foam on the mechanical properties of porcupine quills *Acta Biomaterialia* **9** 9065–9074
- [5] Tattersall G J, Andrade D V, and Abe A S 2009 Heat exchange from the toucan bill reveals a controllable vascular thermal radiator *Science* **325** 468–470
- [6] Bose S, Roy M, and Bandyopadhyay A 2012 Recent advances in bone tissue engineering scaffolds *Trends in Biotechnology* **30** 546–554
- [7] Sanz-Herrera J A, García-Aznar J M, and Doblaré M 2009 On scaffold designing for bone regeneration: a computational multiscale approach *Acta Biomaterialia* **5** 219–229
- [8] Kang H, Lin C Y, and Hollister S J 2010 Topology optimization of three dimensional tissue engineering scaffold architectures for prescribed bulk modulus and diffusivity *Structural and Multidisciplinary Optimization* **42** 633–644

- [9] Dias M R, Guedes J M, Flanagan C L, Hollister S J, and Fernandes P R 2014 Optimization of scaffold design for bone tissue engineering: a computational and experimental study *Medical Engineering & Physics* **36** 448–457
- [10] Cox S C, Thornby J A, Gibbons G J, Williams M A, and Mallick K K 2015 3D printing of porous hydroxyapatite scaffolds intended for use in bone tissue engineering applications *Materials Science and Engineering: C* **47** 237–247
- [11] Luo Y, Zhai D, Huan Z, Zhu H, Xia L, Chang J, and Wu C 2015 3D printing of hollow struts-packed bioceramic scaffolds for bone regeneration *ACS Applied Materials & Interfaces* **8** 1–11
- [12] Leukers B, Güllkan H, Irsen S H, Milz S, Tille C, Schieker M, and Seitz H 2005 Hydroxyapatite scaffolds for bone tissue engineering made by 3D printing *Journal of Materials Science: Materials in Medicine* **16** 1121–1124
- [13] Cho J, Park C S, Kim Y J, and Kim K G 2015 Clinical application of solid model based on trabecular tibia bone CT images created by 3D printer *Healthcare Informatics Research* **21** 201–205
- [14] Vlahinić I, Andò E, Viggiani G, and Andrade J E 2014 Towards a more accurate characterization of granular media: extracting quantitative descriptors from tomographic images *Granular Matter* **16** 9–21
- [15] Al-Raoush R 2007 Microstructure characterization of granular materials *Physica A: Statistical Mechanics and its Applications* **377** 545–558
- [16] Wong H, Head M, and Buenfeld N 2006 Pore segmentation of cement-based materials from backscattered electron images *Cement and Concrete Research* **36** 1083–1090
- [17] Silin D B, Jin G, and Patzek T W 2003 Robust Determination of the Pore Space Morphology in Sedimentary Rocks *SPE Annual Technical Conference and Exhibition* Society of Petroleum Engineers
- [18] Homberg U, Baum D, Prohaska S, Kalbe U, and Witt K 2012 Automatic extraction and analysis of realistic pore structures from μ CT data for pore space characterization of graded soil *Proceedings of the 6th International Conference on Scour and Erosion (ICSE-6)* 345–352
- [19] Thompson K E, Willson C S, and Zhang W 2006 Quantitative computer reconstruction of particulate materials from microtomography images *Powder Technology* **163** 169–182
- [20] Meyer F 1994 Topographic distance and watershed lines *Signal Processing* **38** 113–125
- [21] Roerdink J B T M and Meijster A 2001 The watershed transform: definitions, algorithms and parallelization strategies *Fundamenta Informaticae* **41** 187–228
- [22] Lindquist W B, Lee S M, Coker D A, Jones K W, and Spanne P 1996 Medial axis analysis of void structure in three-dimensional tomographic images of porous media *Journal of Geophysical Research* **101** 8297–8310
- [23] Fouard C, Malandain G, Prohaska S, and Westerhoff M 2006 Blockwise processing applied to brain microvascular network study *Medical Imaging, IEEE Transactions on* **25** 1319–1328
- [24] Butscher A, Bohner M, Roth C, Ernstberger A, Heuberger R, Doeblin N, Von Rohr P R, and Müller R 2012 Printability of calcium phosphate powders for three-dimensional printing of tissue engineering scaffolds *Acta Biomaterialia* **8** 373–385
- [25] Zocca A, Gomes C M, Bernardo E, Müller R, Günster J, and Colombo P 2013 LAS glass-ceramic scaffolds by three-dimensional printing *Journal of the European Ceramic Society* **33** 1525–1533
- [26] Podshivalov L, Gomes C M, Zocca A, Guenster J, Bar-Yoseph P, and Fischer A 2013 Design, analysis and additive manufacturing of porous structures for biocompatible micro-scale scaffolds *Procedia CIRP* **5** 247–252
- [27] Hutmacher D W 2000 Scaffolds in tissue engineering bone and cartilage *Biomaterials* **21** 2529–2543
- [28] Jones M W, Bærentzen J A, and Šrámek M 2006 3D distance fields: a survey of techniques and applications *IEEE Transactions on Visualization and Computer Graphics* **12** 581–599
- [29] Homberg U, Baum D, Wiebel A, Prohaska S, and Hege H C 2014 Definition, extraction, and validation of pore structures in porous material *Topological Methods in Data Analysis and Visualization III* Springer
- [30] Beucher S 1994 Watershed, hierarchical segmentation and waterfall algorithm *Mathematical morphology and its applications to image processing* Springer 69–76
- [31] Pudney C 1998 Distance-ordered homotopic thinning: a skeletonization algorithm for 3D digital images *Computer Vision and Image Understanding* **72** 404–413
- [32] Kaufman A, Cohen D, and Yagel R 1993 volume graphics *IEEE Computer* **26** 51–64
- [33] Amanatides J and Woo A 1987 A fast voxel traversal algorithm for ray tracing *Proc. Eurographics '87* 1–10
- [34] Stalling D, Westerhoff M, and Hege H C 2005 Amira: a highly interactive system for visual data analysis *The Visualization Handbook* Elsevier 749–767